Majidi, S.H., and Beckermann, C., "Modeling of Air Entrainment During Pouring of Steel Castings," in Proceedings of the 70th SFSA Technical and Operating Conference, Paper No. 4.8, Steel Founders' Society of America, Chicago, IL, 2016.

Modeling of Air Entrainment During Pouring of Steel Castings

Seyyed Hojjat Majidi and Christoph Beckermann

Department of Mechanical and Industrial Engineering
The University of Iowa, Iowa City, 52242

Abstract

Air entrainment during mold filling is known to be a major source of reoxidation inclusions in steel castings. A model is developed to predict the location and rate of air entrainment as part of a standard mold filling simulation. The local air entrainment rate is calculated as a function of the turbulent kinetic energy and the magnitude of the normal velocity gradient of the liquid metal at the liquid-air interface. The turbulent kinetic energy is estimated from the sum of the squares of the fluctuating velocity components relative to a spatially averaged mean velocity. The air entrainment model is implemented in a casting simulation software and validated by comparing its predictions to experimental air entrainment measurements for a circular water jet plunging into a quiescent liquid pool. The model is then applied to study the effect of gating system design and pouring parameters on air entrainment in steel casting. It is found that a metal stream from the ladle that is centered above the pouring cup or the use of an offset pouring basin, low head heights, high flow rates, a pressurized gating system, and bottom ingates reduce the amount of entrained air.

1. Introduction

Reoxidation inclusions are among the most commonly reported defects in steel castings. These inclusions affect the surface quality, machinability, and mechanical performance of a cast part. The removal of reoxidation inclusions from castings, if possible, can be very costly. Reoxidation inclusions form when the deoxidized steel comes into contact with oxygen during mold filling. Numerous efforts have been made to minimize reoxidation inclusions in steel castings, but methods to predict reoxidation inclusion formation and generally valid gating design guidelines are currently not available.

Air entrainment during mold filling is the main source of the oxygen that is consumed in reoxidation inclusion formation. In free surface flows, air is entrained at surface discontinuities. Such surface discontinuities are created, for example, by a liquid jet plunging into a pool (Figure 1), breaking waves, or a hydraulic jump, in which a fast moving liquid discharges into a low velocity atmosphere. In the plunging jet case, the air is entrained in a thin layer around the perimeter of the jet where it enters the pool. The air entrainment rate depends primarily on the jet velocity, diameter and turbulence level. Air entrainment commences only above a certain critical jet velocity (approximately 1 m/s for water). For jet velocities at the point of impact of the order of 5 m/s, relative air entrainment rates of one cubic meter of air per cubic meter of water flowing are easily reached.

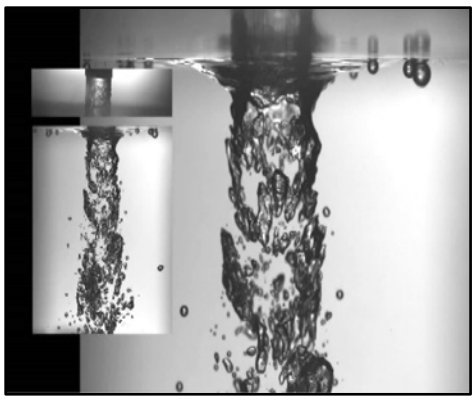

Figure 1. Air bubbles near a plunging liquid water jet. Reprinted from “Air Entrainment Mechanisms in Plunging Jets and Breaking Waves”, by K.T. Kiger and J.H. Duncan, 2012 [1].

During mold filling, several types of free surface flows can occur that entrain air. Liquid metal plunging into the sprue, jets emanating from ingates or falling over edges inside of the casting cavity, and returning waves in runners are some of the most important examples of such flows. The oxygen in that entrained air will almost immediately react with elements in the liquid steel to form solid, liquid, and/or gaseous oxides. While the gaseous oxides can often escape from the casting cavity, liquid and solid oxides are transported with the liquid metal and ultimately end up as non-metallic inclusions in the solidified casting. In steel casting, the inclusions are always lighter than the metal and often accumulate on the cope surface. For a typical inclusion composition in steel, Figure 2 shows the inclusion volume fraction as a function of the relative entrained air volume [2]. A relative air entrainment rate of about 3.5 cubic feet of air (at ambient temperature and pressure) per cubic foot of steel, which is easily reached, results in one cubic inch of inclusions per cubic foot of steel.

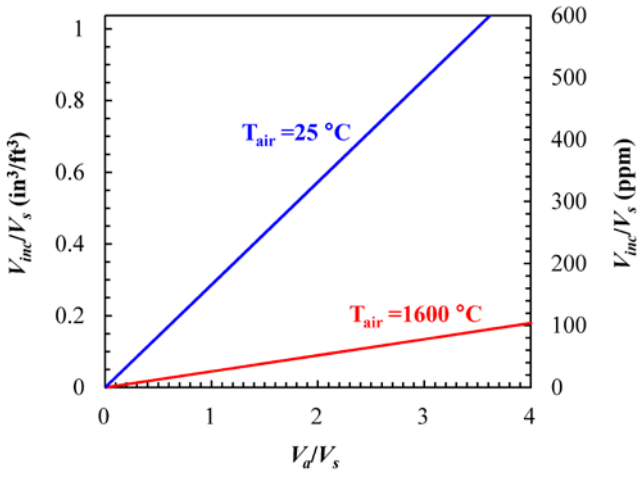

Figure 2. Variation of inclusion volume fraction with relative entrained air volume for carbon/ low-alloy steel [2].

Simulation software is now routinely used in the foundry industry to model not only solidification, but also the filling of the mold with the liquid metal. Such filling simulations are usually one-sided, meaning that they only calculate the flow of the metal but not of the air. Hence, air entrainment is not predicted. Even if the air were included in the calculations, air entrainment and the movement of air bubbles would be difficult to simulate directly because these phenomena occur on such a small scale that they cannot be resolved by a typical computational mesh used in a casting simulation. In the present study, a sub-grid model is implemented into a standard (one-sided) casting filling simulation code to calculate air entrainment rates in free surface flows. The model is validated and calibrated by comparing predicted air entrainment rates for a plunging water jet with previously obtained experimental data. The model capabilities are then demonstrated by simulating the flow in typical casting filling systems and calculating the air entrainment rates. It is shown how different pouring conditions and gating designs affect the rate of entrained air and, hence, the formation of reoxidation inclusions.

2. Model Description

The air entrainment calculations described here are performed as part of a standard casting filling simulation [7]. The filling simulation calculates the melt velocity by solving the Navier-Stokes equations at each time step, while the geometry of the free surface at each time step is determined using a volume tracking method (VOF method). This section describes the model for predicting the air entrainment rate at free surfaces.

The present model is based on the recent work of Ma et al. [4, 5, 10], in which the local air entrainment rate is calculated as a function of the turbulent kinetic energy and the magnitude of the normal velocity gradient at the liquid-air interface. Turbulence inside of the liquid results in disturbances on the free surface. As shown in Figure 3, for a turbulent eddy of size l_e and velocity u_e the disturbance size δ is of the order of

$$\delta \sim \frac{u_e^2}{2g} \quad \rightarrow \quad \delta \sim \frac{k}{g} \tag{1}$$

where k (m^2/s^2) is the turbulent kinetic energy and g (m/s^2) is the gravitational acceleration [3]. Assuming that all of the air entrainment occurs in a layer close to the interface where the disturbances exist, the volumetric rate of entrained air per unit interfacial area, q (m/s), can be estimated by the air quantity passing the inward surface Γ_e in Figure 3 as [4, 5]

$$q(\boldsymbol{x}) \propto u_n(\boldsymbol{x} + \boldsymbol{n} C_1 \delta) - u_n(\boldsymbol{x}) \tag{2}$$

where u_n is the liquid velocity normal to the liquid-air interface, $\boldsymbol{n}$ is the unit normal vector towards the liquid, C_1 is a non-dimensional constant of $\mathrm{O}(1)$, and $\boldsymbol{x}$ is an arbitrary point on the interface.

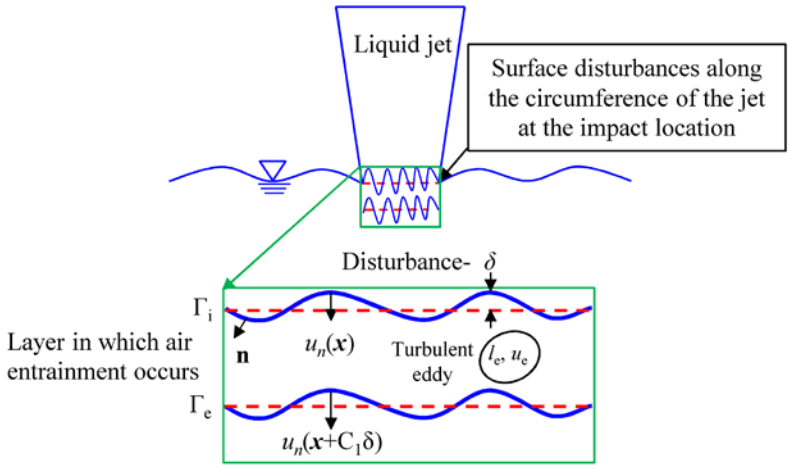

Figure 3. Air entrainment along the periphery of a liquid jet plunging into a quiescent pool. Adapted from "A Comprehensive Sub-Grid Air Entrainment Model for RANS Modeling of Free-Surface Bubbly Flows" by Ma et al. [4].

Using the definition of a derivative

$$\frac{\partial u_n}{\partial n} = \lim_{\Delta n \to 0} \frac{u_n(\boldsymbol{x} + \Delta \boldsymbol{n}) - u_n(\boldsymbol{x})}{\Delta \boldsymbol{n}} \tag{3}$$

and combining Equations (1) - (3), the rate of air entrainment per unit interfacial area can be estimated as

$$q(\boldsymbol{x}) = \frac{C_{\text{ent}}}{g} k(\boldsymbol{x}) \frac{\partial u_n}{\partial n}(\boldsymbol{x}) \tag{4}$$

where C_{ent} is a dimensionless entrainment coefficient that is still to be determined and $\partial u_n / \partial n$ is the normal derivative of the normal component of the liquid velocity at the interface (1/s). The sign of $\partial u_n / \partial n$ determines whether air is entrained or not:

- $\partial u_n / \partial n < 0$: normal velocity decreases in the direction normal to the interface; the interface is moving with a higher velocity than the inward surface; therefore, air will be detrained rather than entrained.
- $\partial u_n / \partial n = 0$: normal velocity remains constant in the direction normal to the interface; the interface is moving with the same velocity as the inward surface; air will not be entrained or detrained.
- $\partial u_n / \partial n > 0$: normal velocity increases in the direction normal to the interface; the inward surface is moving with a higher velocity than the interface; the disturbances are drawn into the liquid and then break up into bubbles.

Hence, only positive values of $\partial u_n / \partial n$ will lead to air entrainment. Equation (4) indicates that the rate of air entrainment per unit interfacial area is a function of the disturbance size and the normal derivative of the normal velocity at the interface. Earlier studies had

pointed out the importance of turbulent kinetic energy and differential velocity in determining the rate of air entrainment [6].

The volumetric air entrainment rate, Q_a (m^3/s), can be calculated by integrating the rate of air entrainment per unit interfacial area over the interfacial area

$$Q_a = \iint_{A_s} q \mathrm{d}A \tag{5}$$

where A_s is the interfacial area.

Turbulent Kinetic Energy

The local turbulent kinetic energy *k* is the kinetic energy per unit mass associated with all eddies within the turbulent flow and is defined as

$$k = \frac{1}{2}(\overline{u_x'^2} + \overline{u_y'^2} + \overline{u_z'^2}) \tag{6}$$

where u_x' , u_y' and u_z' are the fluctuating components of the velocity. They are defined as

$$u_x' = u_x - \overline{u_x} \tag{7a}$$
$$u_y' = u_y - \overline{u_y} \tag{7b}$$
$$u_z' = u_z - \overline{u_z} \tag{7c}$$

where the overbar indicates an average. In fluid mechanics, turbulence models are used for estimating the mean flow characteristics of turbulent flows. These turbulence models calculate the local turbulent kinetic energy of the flow field by solving additional equations. When using turbulence models, temporal average values are used. The method suggested here does not require any turbulence model, and for averaging purposes, it uses spatial averaging instead of temporal averaging. The spatial average is calculated as the mean value of a variable over a 27 point computational stencil in three dimensions. For the velocity components, this can be expressed as

$$\overline{u_x} = \frac{\sum_{p=1}^{27} u_{x,p}}{27} \tag{8a}$$
$$\overline{u_y} = \frac{\sum_{p=1}^{27} u_{y,p}}{27} \tag{8b}$$
$$\overline{u_z} = \frac{\sum_{p=1}^{27} u_{z,p}}{27} \tag{8c}$$

Normal derivative of the normal component of velocity at the interface, $\partial u_n / \partial n$

In the casting filling simulation, the free surface is tracked using the VOF method. In this method, the computational cells in which the liquid-air interface resides have a certain liquid volume fraction, α_l, which varies from zero to unity across the interface. Using the liquid volume fraction, the normal vector at the interface and the normal velocity can be calculated, respectively, as

$$\boldsymbol{n} = \frac{\nabla \alpha_l}{|\nabla \alpha_l|} \tag{9}$$

$$u_n = \boldsymbol{u} \cdot \boldsymbol{n} \tag{10}$$

Then, the normal derivative of the normal velocity at the interface can be calculated from

$$\frac{\partial u_n}{\partial n} = \boldsymbol{n} \cdot \nabla u_n \tag{11}$$

With the turbulent kinetic energy $(\boldsymbol{k})$ and normal derivative of the normal velocity $(\partial u_n / \partial n)$ being calculated as described above, the entrainment coefficient (C_{ent}) is the only unknown in Equation (4). It is determined in the next section by comparing predictions of the air entrainment model with experimental measurements for water.

3. Model Calibration and Validation for a Plunging Water Jet

Air entrainment associated with a circular water jet plunging into a quiescent pool has been studied experimentally by numerous researchers [8, 9]. Their experimental data are used here to validate the present air entrainment model and to determine the entrainment coefficient C_{ent}. The plunging water jet simulations were performed for a tank with length and width of 20 cm (8”). The quiescent pool has a height of 20 cm. The jet enters the computational domain at the top through an inlet that represents a nozzle. The falling height (h_j) is the distance between the nozzle exit and the impact location (Figure 4a). An overflow is designed to keep the falling height constant during a simulation. A base case result for a plunging water jet is shown in Figure 4, with the velocity distribution in the jet and the pool plotted in Figure 4a. The computed local air entrainment rate per unit of entrainment coefficient contours plotted in Figure 4b indicate that, as expected, air entrainment is predicted to take place at the periphery of the jet where it impacts the pool. The variation of the total air entrainment rate (per unit of entrainment coefficient) in the entire computational domain is depicted in Figure 4c. It can be seen that after the initial impact of the jet, the total air entrainment rate reaches a steady state, although some fluctuations persist. For the comparison with experimental measurements shown below, the total air entrainment rate per unit of entrainment coefficient, Q_a / C_{ent}, of the plunging jet is taken as the average value during the steady state period, as illustrated in Figure 4c. This average value is divided by the volumetric flow rate of the water, Q_w, to obtain the relative air entrainment rate per unit of entrainment coefficient for a plunging jet.

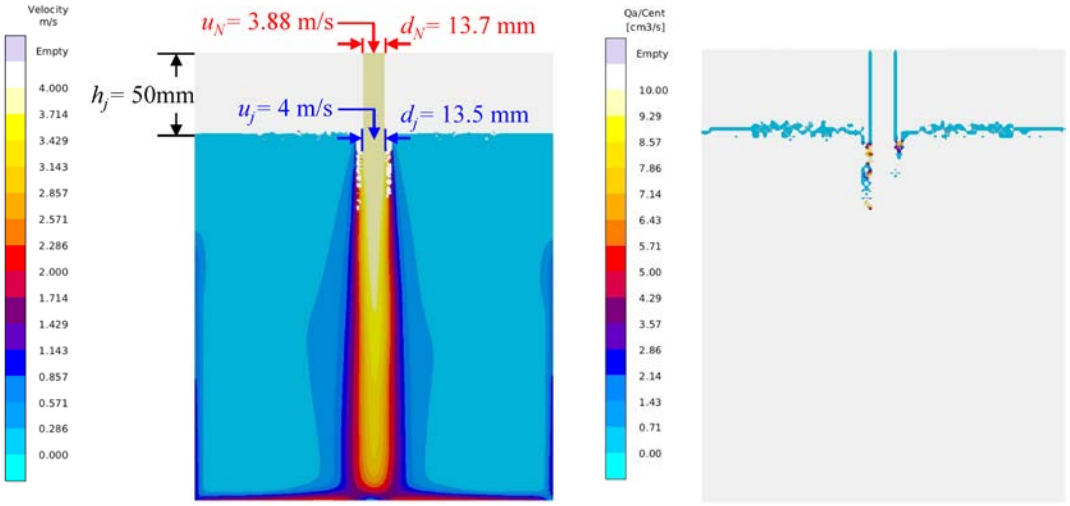

(a) (b)

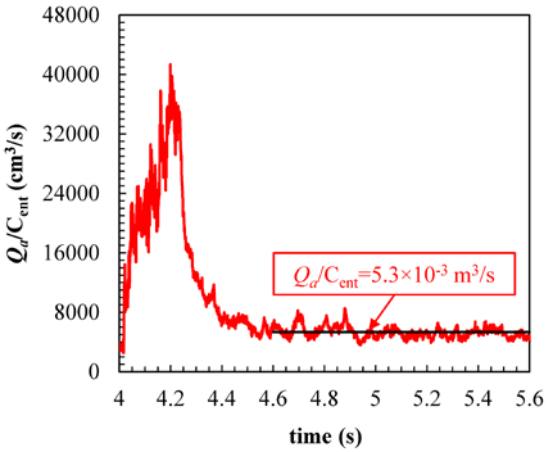

(c)

Figure 4. Base case plunging water jet simulation with $u_j = 4$ m/s, $d_j = 13.5$ mm, and $h_j = 50$ mm: (a) velocity contours at $t = 5$ s at the mid plane, (b) local air entrainment rate per unit of entrainment coefficient contours at $t = 5$ s at the mid plane, and (c) total air entrainment rate per unit of entrainment coefficient as a function of time.

Before determining the entrainment coefficient and comparing the present model to experiments, a computational mesh dependency study was performed. In all cases, a uniform mesh was utilized that consists of cubes of a certain side length. Figure 5 shows that for the plunging water jet base case just discussed, the calculated Q_a / C_{ent} values experience a slight decrease as the mesh is refined from a 3.6 mm to a 1.6 mm grid spacing. This relatively minor mesh dependency was deemed acceptable. At least four grid points are required to numerically resolve the jet itself. A uniform grid spacing of 2 mm is used for all of the following plunging water jet cases.

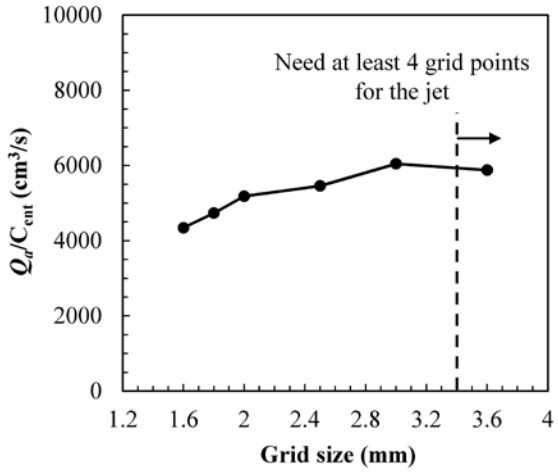

Figure 5. Calculated air entrainment rate per unit of entrainment coefficient as a function of grid spacing for the plunging water jet base case.

Studies have shown that, in addition to the turbulence level, the rate of air entrainment in plunging jets is primarily a function of the jet velocity, u_j , and diameter, d_j, at the location of the impact with the pool [8, 9]. In the simulations, they are controlled by the jet velocity and diameter at the nozzle (inlet), u_N and d_N, respectively, as well as by the falling height between the nozzle and the pool, h_j. All of these variables are indicated in Figure 4a. They are related by

$$u_N = \sqrt{u_j^2 - 2gh_j} \tag{12}$$

$$d_N = d_j \sqrt{\frac{u_j}{u_N}} \tag{13}$$

Simulations were conducted for jet velocities in the range $1 \le u_j(\text{m/s}) \le 6$ and jet diameters in the range $10 \le d_j(\text{mm}) \le 25$. The lower limit of the jet velocity range corresponds approximately to the onset of air entrainment, while the upper limit is a transition point above which air entrainment is no longer controlled by interface disturbances [10].

The air entrainment coefficient, C_{ent}, was determined by comparing the predicted steady state relative air entrainment rates to experimental measurements. In this study, the following experimental correlation for a low turbulence plunging jet proposed by Ervine and Ahmed (1982), as reported in Ref. [9], is used in the calibration

$$\frac{Q_a}{Q_w} = 0.003 Fr_j^2 \tag{14}$$

where the jet Froude number at impact, Fr_j, is defined as

$$Fr_j^2 = \frac{u_j^2}{g d_j} \tag{15}$$

By minimizing the root mean square error between the predicted relative air entrainment rate values and the above experimental correlation, the entrainment coefficient was determined to be equal to $C_{ent} = 0.039$. As shown in Figure 6a, the resulting agreement between measured and predicted relative air entrainment rates is excellent over the entire Froude number range investigated in the present study.

The experimental correlation indicates that the relative air entrainment rate varies with the square of the plunging jet velocity at impact. Figure 6b shows that this trend is correctly predicted by the present model. For a jet velocity of $u_j = 1$ m/s, the air entrainment rate is measured and predicted to become negligibly small. For a jet velocity of $u_j = 6$ m/s (and $d_j = 13.5$ mm), the relative air entrainment rate approaches unity. The experimental correlation specifies that the relative air entrainment rate is inversely proportional to the jet diameter. Figure 6c shows that the present computations predict this trend as well. Overall, the good agreement between measurements and predictions, for a single value of the air entrainment coefficient, lends considerable confidence to the present model and computations.

Next the effect of the turbulence level of the plunging jet on the relative air entrainment rate is studied using the experimental data of Ervine et al. [8]. The turbulence intensity is defined as

$$I = \frac{\sqrt{\overline{u'^2}}}{\bar{u}} \tag{16}$$

where u is the velocity of the jet, and the prime and the overbar indicate the fluctuating and mean components of the velocity, respectively. In the present simulations, turbulence was induced by applying the following time-dependent sinusoidal velocity profile at the nozzle (inlet)

$$u = \bar{u} + u' = \bar{u}\left[1 + I \times \sin(\omega t)\right] \tag{17}$$

where ω and t are frequency and time, respectively. In accordance with the experimental study of Ervine et al. [8], the frequency was set to $\omega = 65\pi$ and the turbulence intensity to $I = 0.05 = 5\%$. Simulations were conducted for four different mean jet velocities. Figure 7 shows that good agreement is obtained between the measured and predicted relative air entrainment rates for a turbulent plunging jet. For a turbulence intensity of 5%, the relative air entrainment rate increases by a factor of approximately three relative to the low turbulence data of Ervin and Ahmed (1982). Clearly, turbulence is a major factor in air entrainment.

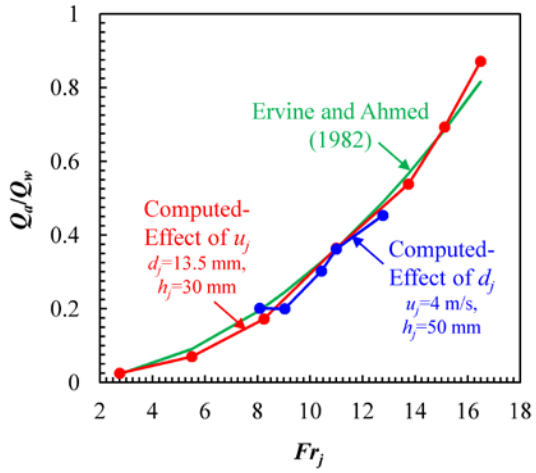

(a)

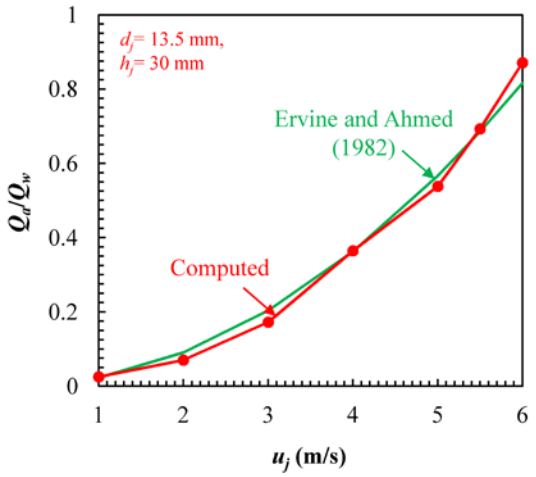

(b)

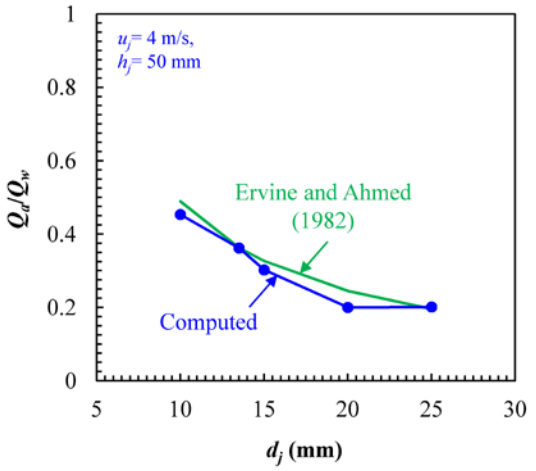

(c)

Figure 6. Relative air entrainment rate for a low turbulence plunging jet as a function of (a) Froude number, (b) jet velocity at impact and (c) jet diameter at impact.

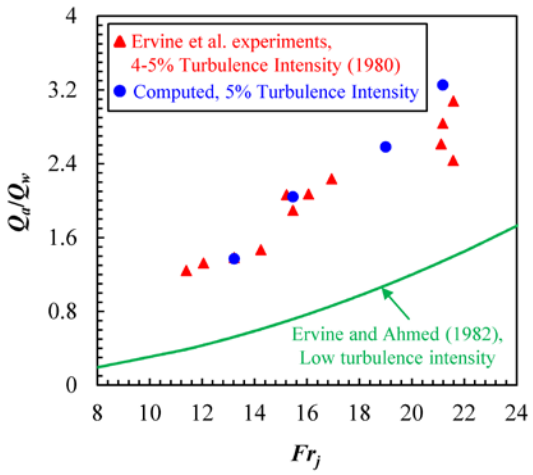

Figure 7. Comparison between measured and predicted relative air entrainment rates for a turbulent plunging jet.

4. Air Entrainment During Mold Filling

The present model is now applied to investigate the effect of various gating system designs and pouring parameters on air entrainment during mold filling. In all cases, the cast part is represented by a rectangular block with a length and width of 30.2 cm (12”) and a height of 17.8 cm (7”). The filling simulations were conducted using a commonly available casting simulation code [7] in which the present air entrainment model was implemented. The material properties were taken from the standard database of the software and correspond to a low alloy steel in a furan sand mold. The pouring temperature was set to 1600 °C (2912 °F). A uniform mesh consisting of cubes with a side length of 3 mm was used in all simulations.

Table 1 lists all of the cases studied. First, a cone shaped pouring cup on top of a vertical down sprue with a cylindrical well and a bottom ingate is investigated. The effects of the gating system pressurization state, fill time (flow rate), location of the impact of the stream from the ladle, and the head height above the cup are studied. Second, air entrainment for an offset pouring basin is examined. Third, the effect of the location of the ingate is studied.

Cone Pouring Cup with Bottom Ingate

The geometry for the gating system with a cone shaped pouring cup and a bottom ingate is provided in Figure 8. The casting has a pour weight of 156 kg (344 lb). First, a non-pressurized and pressurized gating system are compared. As shown in Figure 9, the non-pressurized gating system features an ingate that has twice the cross-sectional area of the sprue (1:2 sprue to ingate area ratio). For the pressurized gating system, the ingate is made smaller in an attempt to keep the upstream part of the gating system filled with

liquid metal during the majority of the filling process; here the area ratio is 1:0.6 (sprue to ingate). The effect of the liquid metal flow rate and, hence, the mold filling time on air entrainment and reoxidation inclusion generation has been a controversial topic in the steel foundry industry for some time. Higher flow rates cause higher velocities in the gating system, but also reduce the time the steel is exposed to oxygen. The pressurization state or degree the gating system is filled with liquid metal during pouring also depends on the flow rate. The two flow rates that are studied here are $Q_s = 1000$ cm^3/s ($t_{fill} = 20$ s) and $Q_s = 625$ cm^3/s ($t_{fill} = 32$ s). Air entrainment can also be expected to be affected by the location where the metal stream from the ladle impacts the cone pouring cup. As illustrated in Figure 10a, a side impact and a center impact are examined. Finally, the effect of the (head) height of the stream from the ladle above the pouring cup on air entrainment is studied. As can be seen in Figure 10b, heights of $H = 2$" and $H = 8$" are examined. Table 1 shows that all combinations of these cases were simulated, resulting in a total of 16 cases featuring the cone pouring cup with a bottom ingate.

Table 1. Overview of the cases simulated for air entrainment in steel casting.

	Trial	Gating Arrangement	Pouring Cup/Basin	Impact Location	Pouring Rate, Q_s (cm^3/s)	Head Height, H (in)
Non-Pressurized	1	Bottom	Cone cup	Side	1000	8”
	2	Bottom	Cone cup	Side	1000	2”
	3	Bottom	Cone cup	Side	625	8”
	4	Bottom	Cone cup	Side	625	2”
	5	Bottom	Cone cup	Center	1000	8”
	6	Bottom	Cone cup	Center	1000	2”
	7	Bottom	Cone cup	Center	625	8”
	8	Bottom	Cone cup	Center	625	2”
	9	Bottom	Offset basin	Side	1000	8”
Pressurized	10	Bottom	Cone cup	Side	1000	8”
	11	Bottom	Cone cup	Side	1000	2”
	12	Bottom	Cone cup	Side	625	8”
	13	Bottom	Cone cup	Side	625	2”
	14	Bottom	Cone cup	Center	1000	8”
	15	Bottom	Cone cup	Center	1000	2”
	16	Bottom	Cone cup	Center	625	8”
	17	Bottom	Cone cup	Center	625	2”
	18	Bottom	Offset basin	Side	1000	8”
	19	Side	Cone cup	Side	1000	8”
	20	Top	Cone cup	Side	1000	8”

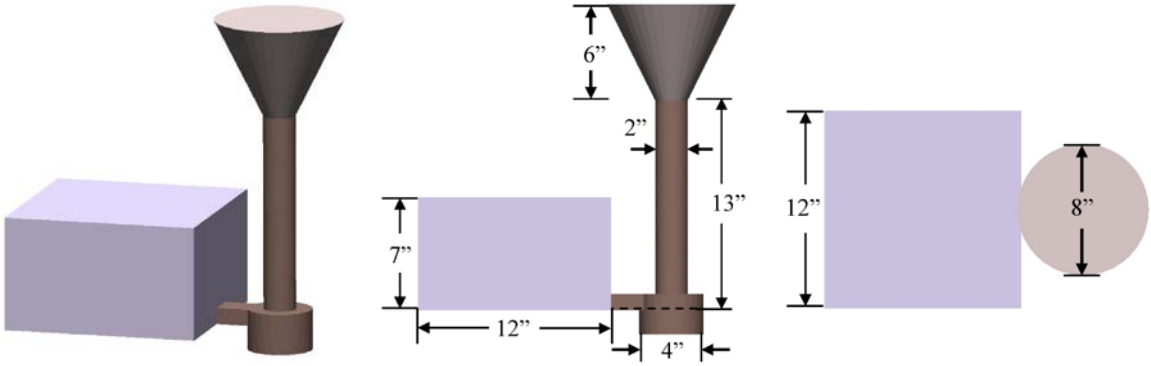

(a) (b) (c)

Figure 8. Gating system and casting geometry for the cone pouring cup with bottom ingate cases: (a) isometric view, (b) front view and (c) top view.

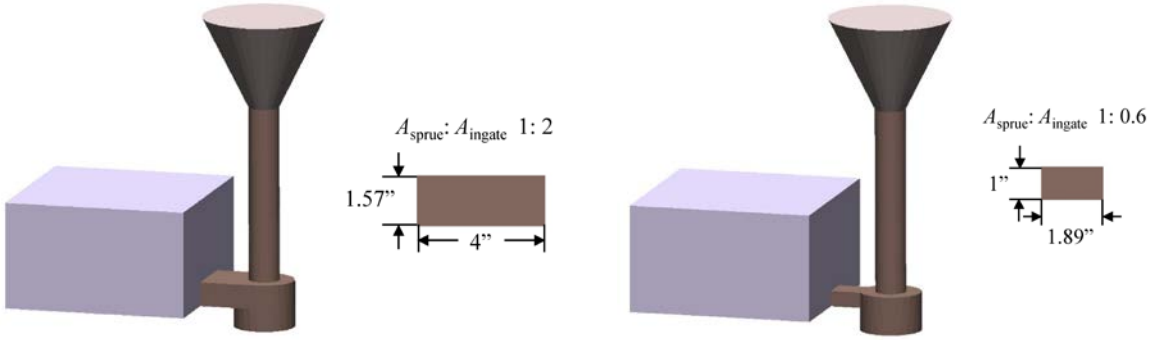

(a) (b)

Figure 9. Ingate geometry for (a) the non-pressurized gating system and (b) the pressurized gating system.

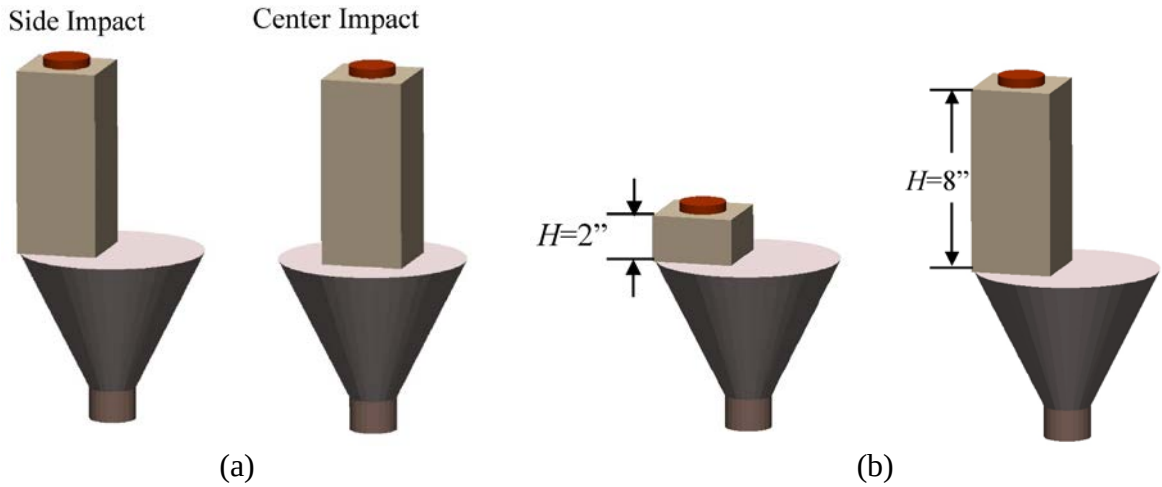

(a) (b)

Figure 10. Geometries for (a) the side and center impact locations and (b) the two different head heights.

Figure 11 shows a comparison of the air entrainment predictions for the non-pressurized and pressurized gating systems. The comparison is made for both side impact (Figure 11a) and center impact (Figure 11b). In all cases, the initial impact of the stream from the ladle onto the cone pouring cup (for side impact) or the bottom of the sprue (for center impact) causes a large spike in the relative air entrainment rate during the first second of filling. This spike is larger for center impact, because the initial falling height (and, hence, plunging jet velocity) is larger for center than for side impact. Smaller secondary spikes can be observed at later times, which can be associated with additional plunging and splashing events. After the initial spike, the air entrainment rate is relatively constant (aside from the fluctuations), although in some cases it decreases slightly until the end of filling. The fluctuations during this period are not due to turbulence of the incoming stream from the ladle, but are generated inside the mold cavity due to unsteadiness of the flow. They are generally larger for the non-pressurized than for the pressurized gating system, indicating that the flow is steadier for a pressurized gating system. Most importantly, during the vast majority of the filling process, the air entrainment rate

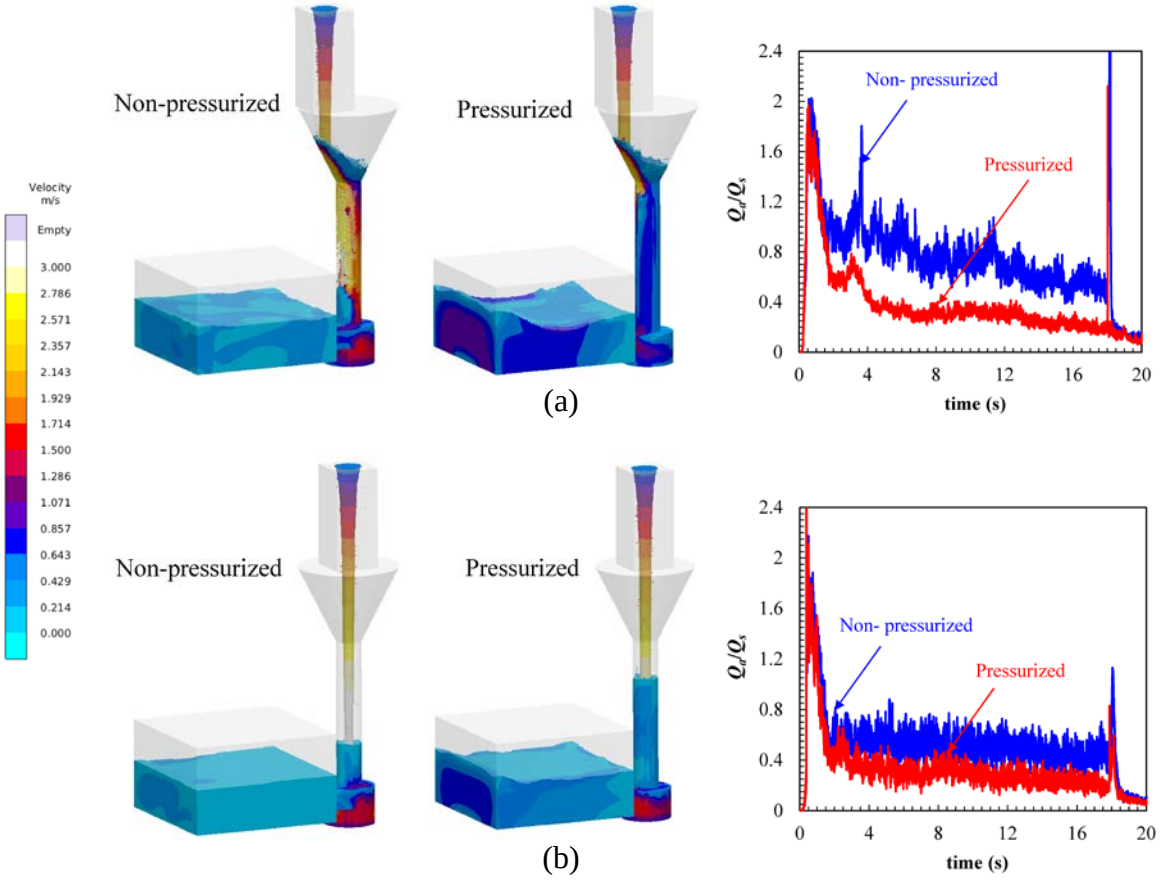

Figure 11. Effect of the gating system pressurization state on the variation of the relative air entrainment rate (plots on the right) for $Q_s = 1000$ cm^3/s ($t_{fill} = 20$ s) and $H = 8$": (a) side impact, (b) center impact. The velocity contours are shown at a time of 10 s.

is significantly smaller for the pressurized than for the non-pressurized gating system. This can be attributed to the fact that for a pressurized gating system, most of the sprue fills up with liquid metal early during the filling process, causing the falling height from the pouring cup into the sprue to be less on average. A smaller falling height reduces the plunging jet velocity at impact and, hence, the air entrainment rate. For the non-pressurized gating system, the liquid metal level in the sprue is low during the majority of the filling process, resulting in a large falling height, regardless of the impact location.

Figure 12 shows a comparison of the air entrainment predictions for the high and low pouring rates, $Q_s = 1000$ cm^3/s ($t_{fill} = 20$ s) and $Q_s = 625$ cm^3/s ($t_{fill} = 32$ s), respectively. The comparison is made for the pressurized gating system and both side impact and center impact. It can be seen that for side impact (Figure 12a), the relative air entrainment rate throughout the filling process is lower for the higher pouring rate. This can attributed to the fact that for the higher flow rate the gating system fills up more quickly with liquid

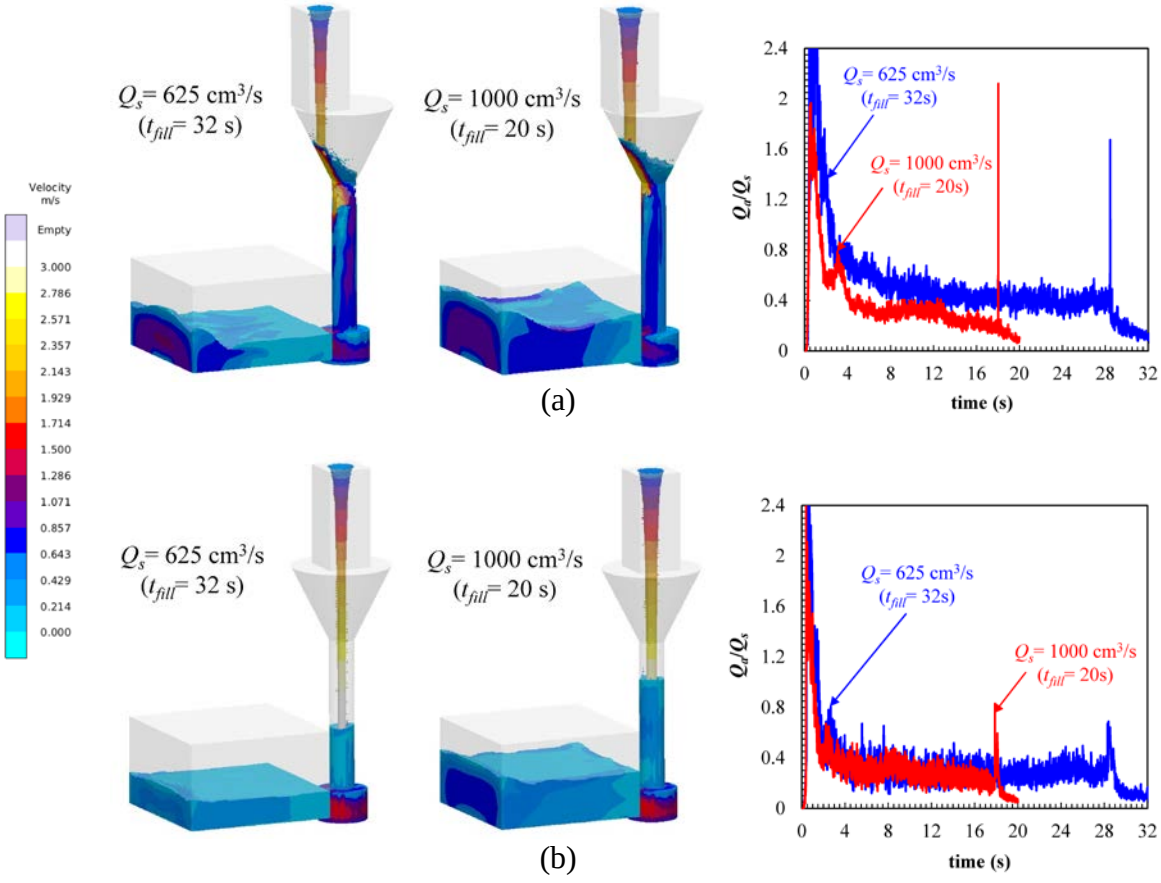

Figure 12. Effect of the liquid metal flow rate, Q_s, on the variation of the relative air entrainment rate (plots on the right) for a pressurized gating system and $H = 8$": (a) side impact, (b) center impact. The velocity contours are shown at a time of 10 s.

metal. In other words, for the higher flow rate the gating system is more pressurized. For the lower flow rate, the ingate would need to be made smaller to achieve the same pressurization state as for the higher flow rate. As already explained in connection with Figure 11, a higher pressurization state causes smaller falling heights and, hence, smaller velocities and air entrainment rates. For center impact (Figure 12b), the difference in the relative air entrainment rate between the two pouring rates is negligibly small. Hence, the effect of lower velocities due to a lower pouring rate is balanced by the effect of higher velocities in the sprue due to a larger falling height.

Figure 13 shows a comparison of the air entrainment predictions for the small and large head heights of the stream from the ladle above the pouring cup, $H = 2$" and $H = 8$", respectively. The comparison is made for the pressurized gating system, the high flow rate, and both side impact (Figure 13a) and center impact (Figure 13b). As expected, a larger head height increases the relative air entrainment rate throughout the pouring process. This can be attributed to a larger falling height causing higher velocities at the point of impact of the stream.

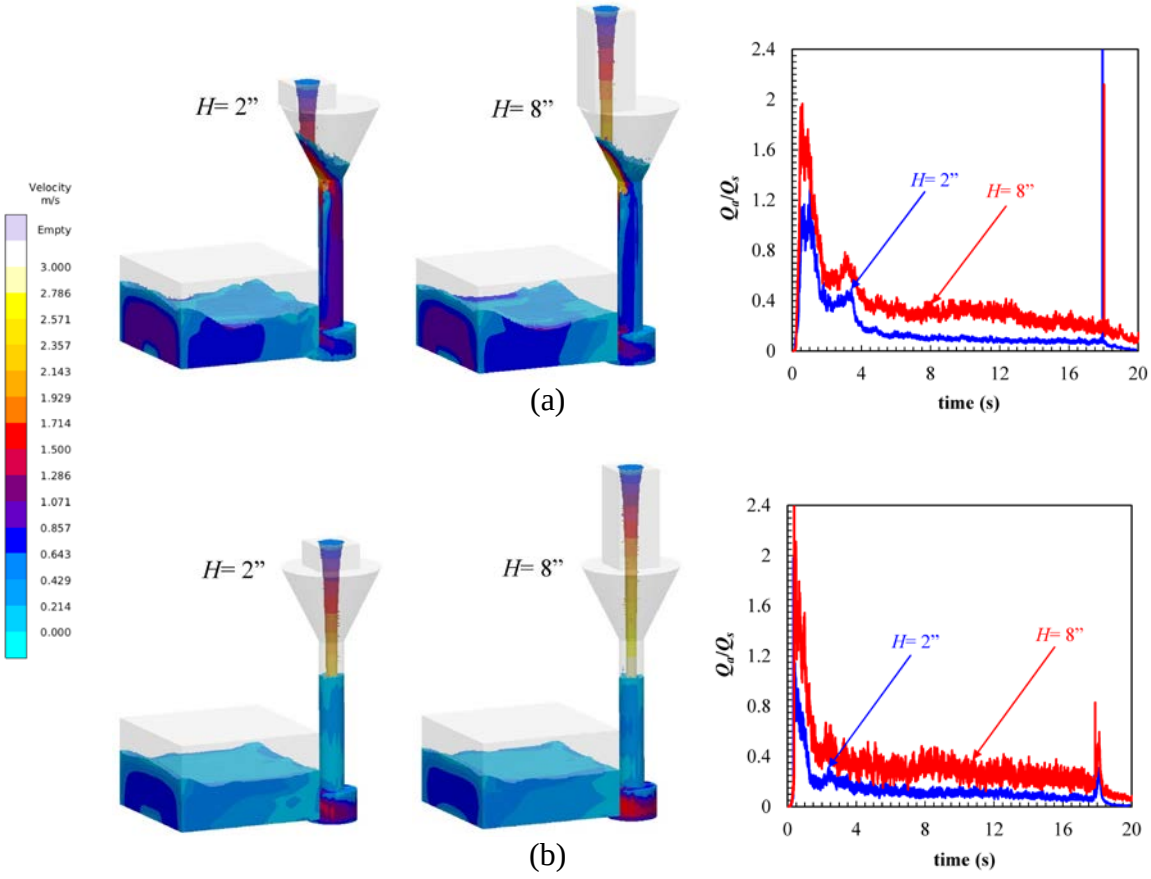

Figure 13. Effect of the head height, H, on the variation of the relative air entrainment rate (plots on the right) for a pressurized gating system and $Q_s = 1000$ cm^3/s ($t_{fill} = 20$ s): (a) side impact, (b) center impact. The velocity contours are shown at a time of 10 s.

Figure 14 shows a comparison of the total volume of air entrained per volume of steel poured for all 16 cases with a cone pouring cup and a bottom ingate. The following conclusions can be drawn. Side impact of the pouring stream on to the pouring cup significantly increases air entrainment compared to center impact, where the stream never impacts the pouring cup. Increasing the head height of the ladle above the pouring cup also increases the amount of air entrained. Reducing the filling time has a beneficial effect on air entrainment and will reduce the amount of reoxidation inclusions generated. Finally, using a pressurized gating system by minimizing the ingate area and keeping the gating system filled with liquid metal throughout the majority of the mold filling process reduces air entrainment. Here, it should be kept in mind that the degree of pressurization of a given gating system depends on the flow rate during filling (fill time). For center impact, pressurization is not nearly as beneficial as for side impact. The merits of gating system pressurization have also been noted by Campbell [11]. It is important to mention that the amount of air entrained differs by almost a factor of 10 between the best and worst case in Figure 14.

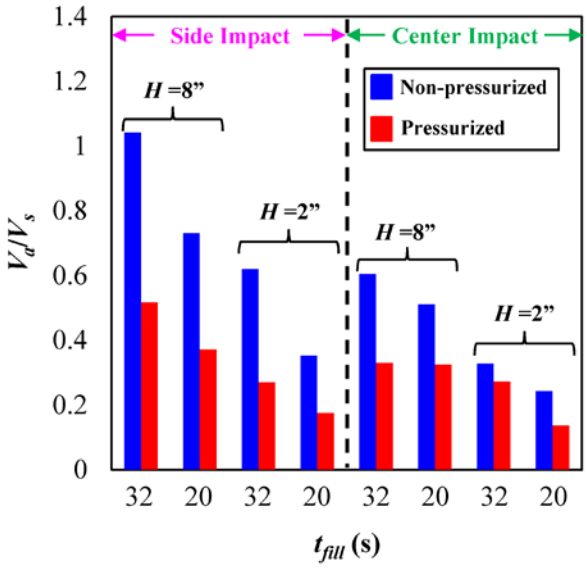

Figure 14. Comparison of the predicted total relative entrained air volumes for the 16 cases with a cone pouring cup and bottom ingate.

Offset Pouring Basin

Campbell [11] has suggested the use of an offset pouring basin in gravity casting to reduce air entrainment. Figure 15 shows a design for an offset pouring basin that was patterned after Ref. [11] and sized to fit with the present casting. Filling simulations were conducted for the offset pouring basin with a bottom ingate and $Q_s = 1000$ cm^3/s and $H = 8$".

Figure 16 shows a comparison of the air entrainment rate predictions for the offset pouring basin with the cone pouring cup for both side and center impact. The comparison

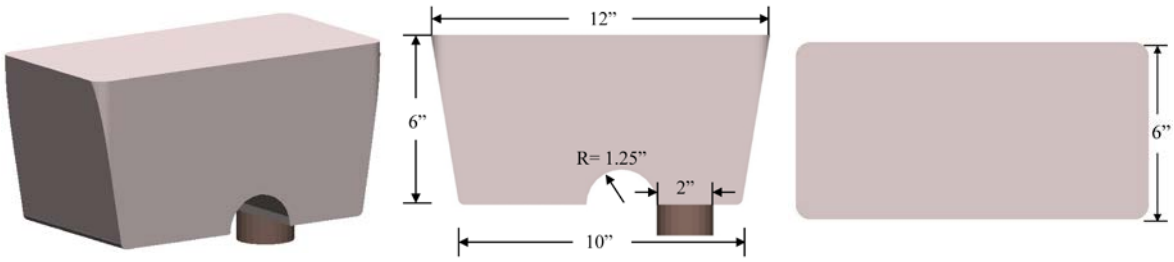

Figure 15. Geometry of the offset pouring basin: (a) isometric view, (b) front view, and (c) top view.

is made for both the pressurized (Figure 16b) and the non-pressurized (Figure 16c) gating system. In both cases, the air entrainment rate for the offset pouring basin is significantly lower than for the cone pouring cup. During the first 4 seconds of filling, the relative air entrainment rate for the offset basin shows two peaks. The first peak is due to the metal stream from the ladle impinging onto the offset portion of the basin, while the second peak is due to the liquid metal from the basin plunging into the empty sprue. The fluctuations in the air entrainment rate for the offset basin are significantly less than for the cone cup, indicating that an offset basin aids in making the filling flow steadier. Note that the filling process takes about 4 seconds longer for the offset basin, since it is larger than the cone cup. Figure 16d shows a comparison of the total volume of entrained air per volume of steel. For the non-pressurized gating system, the use of an offset pouring basin reduces the amount of entrained air by a factor of about 2 relative to a cone cup with center impact and a factor of about 3 relative to a cone cup with side impact. For the pressurized gating system, the beneficial effect of the offset pouring basin is not nearly as strong, but still a factor of about 2 relative to the cone cup with side impact and a factor of about 1.6 relative to the cone cup with center impact.

Ingate Location

Gating a casting from the bottom is preferred in the foundry industry, but it requires a relatively long sprue and special molding techniques (e.g., tiles). Sometimes, the ingates are located on the side of the casting to take advantage of the presence of the mold parting surface. Since the parting surface is usually near the mid-height of the casting, the liquid metal will often fall over considerable heights inside the casting cavity. Such “waterfalls” inside of the mold cavity can be a large source of air entrainment. Clearly, gating a casting from the top is the least desirable configuration from an air entrainment point of view, since it leads to the largest falling heights inside the mold cavity. In order to demonstrate the effect of different ingate locations on air entrainment, filling simulations were conducted for the three geometries shown in Figure 17. Figure 17a depicts the same bottom gated casting that was used in the previous parametric studies. The ingate for the casting in Figure 17b is located at the mid-height of the casting, while the casting in Figure 17c is gated at the top. The length of the sprue and all other features were kept the same for all three ingate locations in order to allow for a more direct comparison between the different cases.

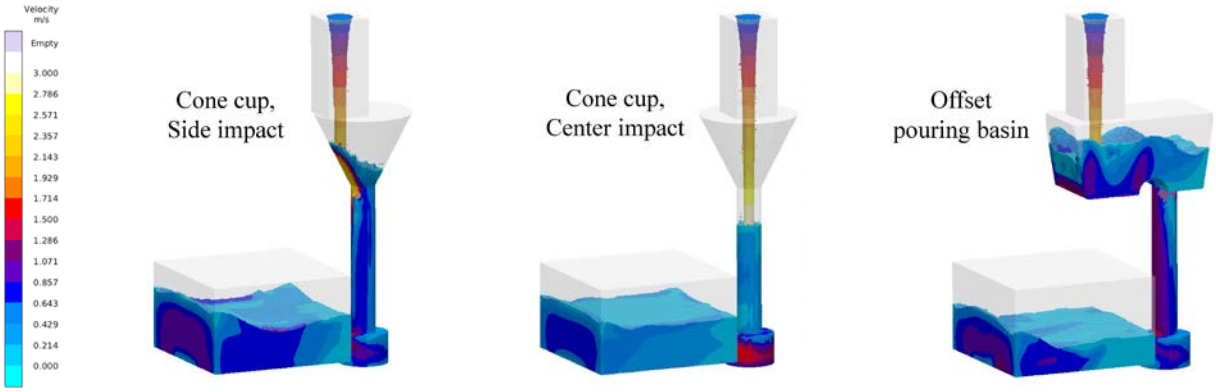

(a)

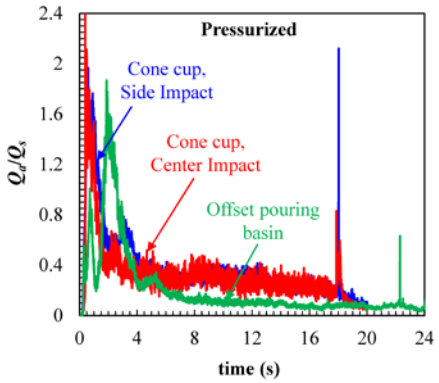

(b)

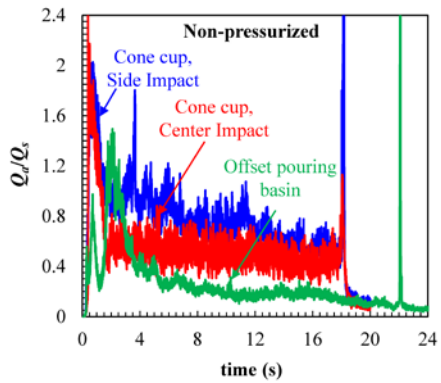

(c)

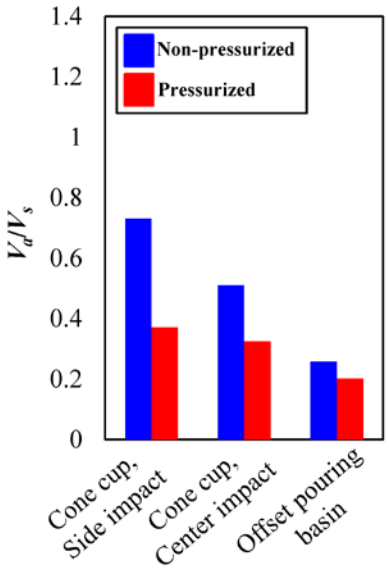

(d)

Figure 16. Comparison of the offset pouring basin with the cone pouring cup (side and center impact) for $Q_s = 1000$ cm^3/s and $H = 8$ ": (a) velocity contours at $t = 10$ s for a pressurized gating system, (b) variation of the relative air entrainment rates for a pressurized gating system, (c) variation of the relative air entrainment rates for a non-pressurized gating system, and (d) predicted total relative entrained air volumes.

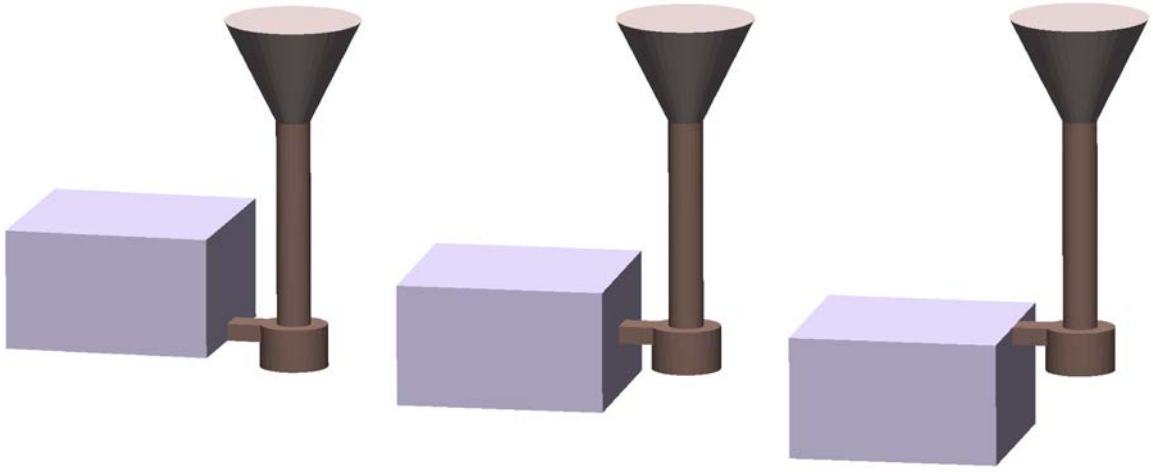

(a) (b) (c)

Figure 17. Geometries for the different ingate location cases: (a) bottom gated, (b) side gated, and (c) top gated.

Figure 18 shows a comparison of the air entrainment rate predictions for the three different ingate locations. The comparison is made for the cone pouring cup with side impact, pressurized gating system, $Q_s = 1000$ cm^3/s ($t_{fill} = 20$ s), and $H = 8$". It can be seen that the ingate location significantly affects air entrainment during mold filling. For the side and top gated castings, a strong jet of liquid metal emanates from the ingate and plunges onto the bottom surface of the casting cavity during large portions of the filling process (Figure 18a). The associated splashing inside of the casting cavity causes very high rates of air entrainment (Figure 18b). This air entrainment subsides once the jet from the ingate is fully submerged. Figure 18c indicates that the total volume of entrained air for the side ingate is almost 2.5 times larger than for the bottom ingate. For the top ingate the entrained air volume is more than 5 times larger than for the bottom ingate. Clearly, to produce clean steel castings large "waterfalls" inside of the casting cavity are to be avoided.

5. Conclusion

A model is developed to predict the location and rate of air entrainment as part of a standard mold filling simulation. The local air entrainment rate is calculated as a function of the turbulent kinetic energy and the magnitude of the normal velocity gradient of the liquid metal at the liquid-air interface. The air entrainment model is implemented in a casting simulation software and validated by comparing its predictions to experimental air entrainment measurements for a water jet plunging into a pool. Excellent agreement is obtained over a large range of jet velocities, diameters, and turbulence levels. The model is then applied to study the effect of gating system design and pouring parameters on air entrainment in steel casting. It is found that a metal stream from the ladle that is centered above the pouring cup or the use of an offset pouring basin, low head heights, high flow rates, a pressurized gating system, and bottom ingates reduce the amount of entrained air.

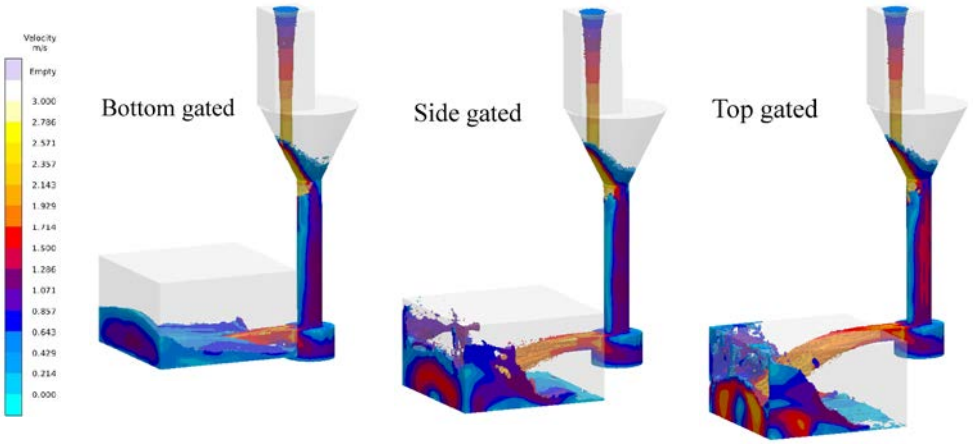

(a)

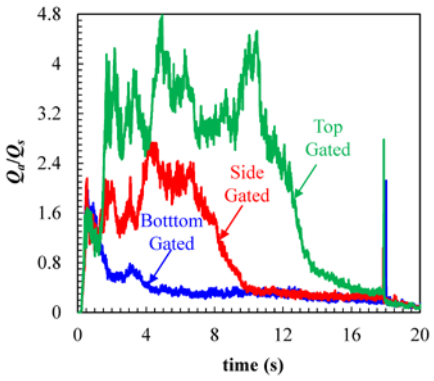

(b)

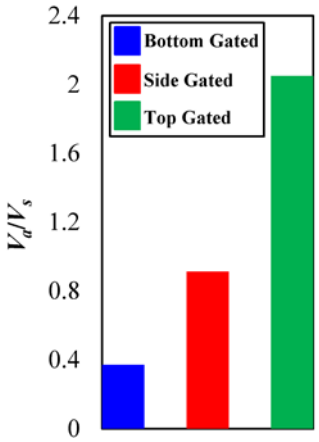

(c)

Figure 18. Effect of the ingate location for $Q_s = 1000$ cm^3/s ($t_{fill} = 20$ s), $H = 8$ ", pressurized gating system, cone pouring cup, and side impact: (a) velocity contours at a time of 4 s, (b) variation of the relative air entrainment rates, and (c) comparison of the predicted total relative entrained air volumes.

While the results of the present mold filling simulations provide some guidance, every casting is different and requires careful design of the gating system to minimize air entrainment. It is hoped that the computer simulation model developed in this study allows foundries to evaluate different gating designs and pouring parameters before the first casting is poured.

Future work will include further experimental validation of the air entrainment model. The present model was calibrated for a plunging water jet only. It is not entirely clear if it provides quantitatively accurate air entrainment predictions for other flow configurations (e.g., breaking waves) and for liquid metals. Furthermore, the present model will be linked to a reoxidation inclusion generation and transport model, in a manner similar to the one by Melendez et al. [2]. Using such a combined model allows for the prediction of the reoxidation inclusion sizes, number densities, and locations in a solidified casting.

References

1. K.T. Kiger and J.H. Duncan, “Air Entrainment Mechanisms in Plunging Jets and Breaking Waves”, *Annual Review of Fluid Mechanics*, 2012, Vol. 44, pp. 563-596.
2. A.J. Melendez, K.D. Carlson and C. Beckermann, “Modelling of Reoxidation Inclusion Formation in Steel Casting”, *International Journal of Cast Metal Research*, 2009, Vol. 32, pp. 624-638.
3. J. Hunt, “Turbulent Structure and Turbulent Diffusion near Gas-Liquid Interfaces”, in: W. Brutsaert, G. Jirka (EDS.), Gas Transfer at Water Surfaces, Reidel, Dordrecht, The Netherlands, 1984, Vol. 43, pp. 67-82.
4. J. Ma, A.A. Oberai, D.A. Drew, R.T. Lahey and M. Hyman, “A Comprehensive Sub-Grid Air Entrainment Model for RANS Modeling of Free- Surface Bubbly Flows”, *Journal of Computational Multiphase Flow*, 2011, Vol. 3, pp. 41-56.
5. J. Ma, A.A. Oberai, D.A. Drew and R.T. Lahey, “A Two-Way Coupled Polydispersed Two-Fluid Model for the Simulation of Air Entrainment Beneath a Plunging Liquid Jet”, *Journal of Fluids Engineering*, 2012, Vol. 134, pp. 101304 (10 pages).
6. H. Kobus, “Local Air Entrainment and Detrainment”, in: *Symposium on Scale Effects in Modelling Hydraulic Structures*, 1984, Vol. 4, pp. 1-10.
7. *MAGMAsoft*, MAGMA Gmbh, Kackerstrasse 11, 52072 Aachen, Germany.
8. D.A. Ervine, E. McKeough and E.M. Elsawy, “Effect of Turbulence Intensity on the Rate of Air Entrainment by Plunging Water Jets”, *ICE Proceedings*, 1980, Vol. 69, pp. 425-445.
9. K.J. Sene, “Air Entrainment by Plunging Jets”, *Chemical Engineering Science*, 1988, Vol. 43, pp. 2615-2623.
10. J. Ma, A.A. Oberai, D.A. Drew, R.T. Lahey and F.J. Moraga, “A Quantitative Sub-Grid Air Entrainment Model for Bubbly Flows - Plunging Jets”, *Computers and Fluids*, 2010, Vol. 39, pp. 77-86.
11. J. Campbell, "Complete Casting Handbook: Metal Casting Processes, Techniques and Design", Butterworth-Heinemann; Oxford, London, 2011.